Terahertz saturable absorption from relativistic high-temperature thermodynamics in black phosphorus

Nidhi Adhlakha,[1] Zeinab Ebrahimpour,[1,2] Paola Di Pietro,[1] Johannes Schmidt,[1] Federica Piccirilli,[1] Daniele Fausti,[3,4] Angela Montanaro,[3,4] Emmanuele Cappelluti,[5] Stefano Lupi,[6] and Andrea Perucchi[1,*]

[1] *Elettra-Sincrotrone Trieste S.C.p.A., S.S. 14 km163.5 in AREA Science Park, Trieste 34012, Italy*

[2] *Abdus Salam International Centre for Theoretical Physics, Strada Costiera 11, Trieste I-34151, Italy*

[3] *Department of Physics, Università degli Studi di Trieste, Trieste 34127, Italy*

[4] *Chair of Solid State Physics, Department of Physics, University of Erlangen-Nürnberg, Erlangen 91058, Germany*

[5] *Istituto di Struttura della Materia, CNR (ISM-CNR), Trieste 34149, Italy*

[6] *CNR-IOM and Dipartimento di Fisica, Università di Roma Sapienza, P.le Aldo Moro 2, Roma I-00185, Italy*

(Received 24 May 2023; revised 4 September 2023; accepted 19 October 2023; published 17 November 2023)

Due to its tunable infrared band gap and its anisotropic conduction properties, black phosphorus represents a very unique two-dimensional (2D) material, the potential of which in the engineering of new devices still needs to be fully explored. Here, we investigate the nonlinear terahertz (THz) electrodynamics of black phosphorus along the more conducting armchair direction. Similarly to the case of other 2D systems such as graphene and topological insulators, the THz saturable-absorption properties of black phosphorus can be understood within a thermodynamic model by assuming a fast thermalization of the electron bath. While black phosphorus does not display the presence of massless fermions at ambient pressure and temperature, our analysis shows that its anomalous THz nonlinear properties can be accounted for by a relativistic massive Dirac dispersion, provided that the Fermi temperature is low enough. An optimal tuning of the Fermi level therefore represents a strategy to engineer a strong THz nonlinear response in other massive Dirac materials, such as transition-metal dichalchogenides or high-temperature superconductors.

DOI: 10.1103/PhysRevApplied.20.054039

I. INTRODUCTION

Among the family of two-dimensional (2D) materials, black phosphorus (BP) stands out for its highly distinctive properties. At a fundamental level, BP is a very fascinating material, due to the occurrence of a pressure-induced topological Lifshitz transition, which turns the material from semiconducting to metal [1,2]. Indeed, it is found that at relatively low pressures (approximately 1.5 GPa), a nonavoided band crossing gives rise to a plasma of Dirac massless charge carriers.

On the other hand, BP is also extremely appealing for optoelectronic applications [3], since it couples a significantly high mobility (reaching up to 1000 $cm^2/V.s$) with the presence of an infrared and tunable (0.3–2 eV) band gap [4]. Its unique anisotropic in-plane transport may be further exploited to design devices with completely new functionalities [5,6]. BP is also a hyperbolic photonic material in the THz range [7], a property that can be exploited for a large variety of applications, such as hyperlensing or subdiffraction light confinement. Nonlinear effects are crucial in many optoelectronic applications, such as for ultrafast signal processing [8] or optical sensing [9].

Remarkably, miniaturization and electromagnetic confinement will induce the presence of strong electric fields that may affect BP in a nonlinear way, thus making its optical properties dependent on the characteristics of the applied THz beam. In the dc limit, BP is also known to exhibit nonlinearities, varying from current saturation to impact ionization [10–13].

The physical mechanisms underlying these nonlinearities are still debated and may be intimately connected to the low-frequency limit of the conductivity in the THz regime. The saturation properties in the THz absorption displayed by 2D materials such as graphene or topological insulators have recently been investigated both theoretically and experimentally by making use of high-peak-power THz sources [14,15]. One may thus wonder whether BP, being on the verge of a Lifshitz transition that would

*andrea.perucchi@elettra.eu

eventually give rise to Dirac electrons, may share the same physics.

To answer this question, here we provide a characterization of the nonlinear optical properties of bulk BP as a function of the incoming THz field, by exploiting the high-power TeraFERMI [16,17] source. This characterization serves as a benchmark for theoretical models, which aim to identify the fundamental ingredients responsible for strong THz nonlinear behavior in general.

II. RESULTS AND DISCUSSION

The main result from our investigation is summarized in Fig. 1, where we compare the real part of the linear (low electric THz field) optical conductivity $\sigma_1(\nu)$, as extracted from FTIR reflectivity measurements at the SISSI beam line [18], with the conductivity for three selected high-THz-field intensities. These measurements are performed with THz light polarized along the more conducting *armchair* direction, while results from the *zig-zag* polarization direction are briefly discussed in Appendix C. The THz optical conductivity for all fields presents a weakly metallic behavior due to the presence of dopant defects [2]. We note from Fig. 1(b) that $\sigma_1(\nu)$ is not constant for all incoming THz fields, but progressively decreases as long as the THz electric field value increases.

The optical conductivity can be fitted with one single Drude term, thus allowing us to estimate the plasma frequency (ω_p) and the scattering rate (Γ), as reported in Figs. 1(c) and 1(d). An analysis of the Drude parameters reveals that the observed decrease of $\sigma_1(\nu)$ cannot be simply attributed to an enhanced scattering rate associated with heating effects. On the contrary, the scattering rate decreases for higher fields, an effect previously observed in graphene and attributed to the dominance of long-range scattering on Coulomb impurities [19]. This scenario is even more likely in BP, where significant concentrations of ionized point defects are believed to act as very efficient charge-carrier scattering agents [20].

The decrease of the optical conductivity at high fields is therefore driven by the reduction in the plasma frequency $\omega_p = \sqrt{4\pi Ne^2/m^*}$, where N is the carrier density and the effective mass is defined as $m^* = \hbar^2/\mathrm{d}^2\varepsilon/\mathrm{d}k^2$. The plasma frequency measured along the *armchair* direction varies between 660 cm^{-1} at 0.1 kV/cm to 470 and 300 cm^{-1} at 350 and 1650 kV/cm, respectively. This shows that strong nonlinear effects are already at play between approximately 0.1 and 350 kV/cm.

The effective mass m^* used for the calculation of ω_p is a constant only as long as the charge carriers are restricted to a small portion of the Brillouin zone (BZ) at the bottom of the conduction band, where the parabolic approximation holds. This is, however, no longer true for high accelerating fields, which can drive charge carriers in regions of the BZ where the band dispersion relation is no longer parabolic. This is indeed the case for InSb [21,22] or Bi [23], where the breakdown of the effective-mass approximation explains their saturable-absorption properties in the presence of strong THz fields.

This scenario can be mimicked with a finite-difference time-domain (FDTD) approach, which incorporates the nonlinear effects by making use of a wave-vector-dependent effective mass $m^* = m^*(\boldsymbol{k})$, as in Ref. [21]. As detailed in Appendix E, the calculation qualitatively reproduces the enhancement of the transmitted THz pulses for increasing incoming fields but overestimates the transmission increase, especially for fields higher than 1 MV/cm.

Here, one should keep in mind that FDTD is a purely one-electron model, which incorporates scattering only as a friction parameter in the equation of motion of the quasiclassical electron. However, for sufficiently high fields, both electron-electron and electron-phonon scattering can have dramatic effects on the THz nonlinear properties. As a consequence, in most realistic cases, temperature effects need to be incorporated in some form.

III. THERMODYNAMIC MODEL

The most successful approach used to describe THz nonlinear properties of quantum materials is the thermodynamic model introduced by Mics *et al.* [19] to explain the THz-induced transparency in graphene. Besides reproducing the optical conductivity of graphene at high fields, the thermodynamic model has also demonstrated its validity in modeling the generation of THz harmonics [24] and plasmon-resonance softening both in graphene [25] and in topological insulators [26] in ribbon-array structures. The thermodynamic model assumes that the electrons that are absorbing energy from the THz field quickly exchange energy through electron-electron collinear scattering events [15], while the lattice temperature remains the same. As a consequence of the ultrafast electron heating, the chemical potential readjusts to the increased electron temperature (T_e), thereby lowering its Drude weight.

To check whether the thermodynamic model can be applied to BP as well, we first evaluate the heating induced by the THz pulses. To this aim, we employ a two-temperature model,

$$c_e\rho^{\mathrm{BP}}\frac{\partial T_e}{\partial t} = G(T_l - T_e) + S(t), \tag{1}$$

$$c_l\rho^{\mathrm{BP}}\frac{\partial T_l}{\partial t} = G(T_e - T_l), \tag{2}$$

where $S(t)$ corresponds to the impulsive heat provided by the THz pulse, G is the electron-phonon coupling constant, and $c_e(T)$ and $c_l(T)$ are the electronic and lattice components of the heat capacity. The system of coupled differential equations is solved with the help of the NTMpy software package [27]. The details of the parameters are

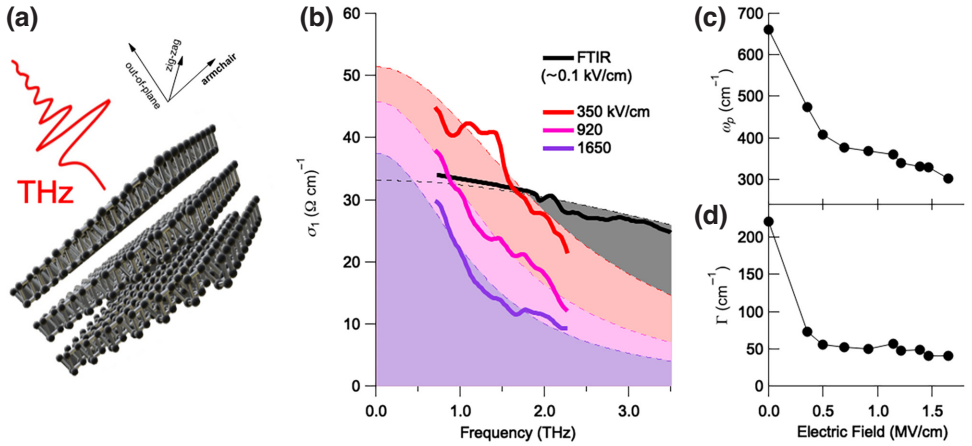

FIG. 1. (a) The BP structure. (b) The real part of the optical conductivity of BP measured along the *armchair* polarization directions at selected THz electric field strengths. The measurement at low THz field (approximately 0.1 kV/cm) was performed with a Fourier-transform infrared (FTIR) spectrometer, while the measurements at selected field strengths were performed by employing the single-cycle pulses from the TeraFERMI facility. The overall behavior of $\sigma_1(\nu)$ can be described (dashed lines) by the Drude model. The optical conductivity decreases when the THz field increases. (c),(d) The (c) THz-field-dependent plasma frequency ω_p and (d) scattering rate Γ, as extracted from the Drude fitting.

provided in Appendix F. We note, however, that the electron heat capacity is evaluated through the textbook formula $c_e(T) = \frac{1}{3}\pi^2 D(\varepsilon_F) k_B^2 T$, where $D(\varepsilon_F) = \frac{3}{2} N/\varepsilon_F$. The Fermi energy $\varepsilon_F = 32$ meV is estimated by making use of low-temperature FTIR data, as described in Appendix D.

The results of the two-temperature model are reported in Fig. 2(a), showing the distribution of the electronic temperature in time and space, along the whole thickness of our BP sample, for the highest THz field (1.65 MV/cm). In order to evaluate an effective temperature for the whole sample, we perform an averaging along the entire sample thickness, weighted by the THz-pulse penetration depth (approximately 6 μm).

The two-temperature model thus allows us to plot the evolution of the Drude spectral weight (SW $= \omega_p^2$) as a function of T_e, ranging from 600 to 2750 K. This can be compared with the T-dependent data from FTIR infrared reflectivity (see Appendix D), covering, on the other hand, T values from 10 to 300 K. The results are reported in [Fig. 2(c)], where the Drude weight is plotted either as a function of T for FTIR or as a function of T_e for the THz-field-dependent data.

Overall, the spectral weight decreases monotonically as a function of temperature, with a striking drop observed between the FTIR and the field-dependent experimental data. The collapse of the spectral weight is remarkable, since at the highest electric field value, corresponding to $T_e \sim 2750$ K, SW(T) has dropped below 20% of its low-temperature value. Interestingly, the Fermi temperature $T_F = 370$ K coincides with the region where the SW(T) decrease is more pronounced. This indicates that T_F sets the temperature scale for the dramatic decrease of the spectral weight.

We now want to theoretically estimate the expected T dependence of the SW. To this aim, we first need to establish the T dependence of the chemical potential $\mu(T)$. Due to the high values of T_e considered here ($T_e \gtrsim 7T_F$), the usual Sommerfeld expansion cannot be employed. $\mu(T)$ is therefore evaluated through a numerical procedure [25] calculating the shift necessary to conserve the total number of charge carriers, according to the Fermi-Dirac distribution (see Appendix G):

$$N(T) = N(T=0) = \int_{-\infty}^{+\infty} g(\varepsilon) f(\varepsilon, \mu(T), T) d\varepsilon, \quad (3)$$

where $f(\varepsilon, \mu(T), T) = (1 + \exp[\varepsilon - \mu(T)/k_B T])^{-1}$ and $g(\varepsilon)$ is the density of states. Once the temperature dependence of the chemical potential has been established, we can calculate SW(T) as

$$\mathrm{SW}(T) \propto \int_{-\infty}^{+\infty} v(\varepsilon)^2 g(\varepsilon) \frac{\partial f(\varepsilon, \mu(T), T)}{\partial \varepsilon} d\varepsilon, \quad (4)$$

where $v(\varepsilon)$ is the electron velocity, defined by $v(\varepsilon) = \partial\varepsilon(k)/\partial k|_{k_0:\varepsilon(k_0)=\varepsilon}$.

It remains to be seen which form of the density of states $g(\varepsilon)$ best reproduces our experimental results. As shown in Fig. 2(b), a parabolic Schrödinger-like dispersion with $m^* = 0.08 m_e$ fits the BP band structure over a rather limited wave-vector range, roughly corresponding to the energy scale set by ε_F. At higher energies, the parabolic dispersion strongly deviates from the real band structure of BP. On the other hand, making use of a massive Dirac dispersion in the form $\varepsilon = \sqrt{m^{*2}c^4 + p^2c^2}$ allows a better matching to the actual BP band structure over an extended energy range, from 0 to 0.4 eV ($k \sim 0 - 1.6$ nm^{-1}).

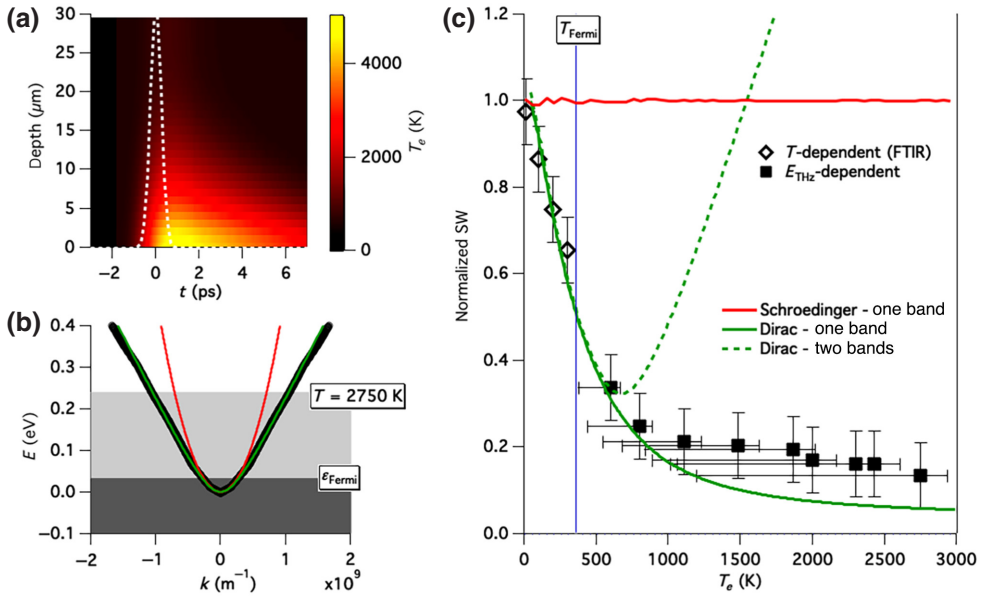

FIG. 2. (a) A false-color representation of the electron temperature as a function of time (horizontal) and penetration inside the sample (vertical), calculated for the *armchair* polarization at the maximum applied THz electric field (1650 kV/cm). The dashed white line is a Gaussian with a full width at half maximum (FWHM) of 590 fs, representing the time profile of the THz source used in the simulation. (b) The energy versus momentum dispersion of BP from Ref. [28] (black) and for two model dispersion relations: Schrödinger (red) and Dirac massive (green). (c) The normalized SW (markers) as a function of T_e, for T-dependent reflectivity (diamonds) and THz-field-dependent data (squares). To take into account possible scattering events occurring in different directions of the k space, we set as a lower bound of T_e, the value obtained from a simulation for an effective "isotropic" electron heat capacity, calculated as a geometrical average over the *armchair* and *zig-zag* directions. The continuous lines correspond to the calculated SW(T) for the two model dispersion relations as in (b). The dashed green line corresponds to the Dirac model, allowing for electron-hole pair formation (see the text).

The choice of the proper band dispersion has a profound impact on the functional dependence of $g(\varepsilon)$ and $v(\varepsilon)$ and therefore on the evaluation of SW(T), as demonstrated in Fig. 2(c). The most striking feature is that the Schrödinger-like parabolic band model predicts a T-independent Drude spectral weight. This is a consequence of the so-called f-sum (or conductivity-sum) rule

$$\mathrm{SW}(T) = \omega_p(T)^2 = 8\int_0^\infty \sigma_1(\nu)d\nu = \frac{4\pi Ne^2}{m^*}, \qquad (5)$$

representing a statement on the conservation of the number of particles. This implies that in a model considering one single (infinite) band in a purely parabolic potential, SW(T) cannot change. It is known, however, that the relation in Eq. (5) is no longer true for Dirac materials [29–31]. In the case of graphene, both the compensated semimetal properties as well as the Dirac nature of the quasiparticles are responsible for the distinctive T dependence of the SW(T) [32].

For an infinite three-dimensional Dirac dispersion, the numerical calculation shown in Fig. 2(c) predicts a dramatic drop of the Drude SW(T), in good agreement with our experimental observation. This shows that the THz nonlinear properties of BP are ruled by the high-temperature ($T > T_F$) thermodynamics of a relativistic Fermi gas [33], which have previously been addressed in the framework of the study of white-dwarf stars, hot quark matter, and gluon-quark plasma, rather than condensed-matter physics.

In this regard, a very interesting question is whether the particle-antiparticle symmetry should be included in our model, by taking into account the thermodynamic equilibration with holes in the valence band. This phenomenon could take place via impact ionization [13], when charge carriers accumulate enough energy from the driving field, so that they can be promoted in the conduction band. We have therefore calculated the thermodynamic SW(T) dependence by taking into account the presence of both electron and hole dispersions. In this case, depicted by the green dashed line in Fig. 2(c), an upturn in SW(T) would be expected at $T_e \sim 600$ K, while SW(T) may even exceed its low-temperature value for $T_e \gtrsim 1500$ K.

This scenario is in disagreement with our experimental findings. We believe that the reason for the discrepancy is that impact ionization is an avalanche phenomenon requiring the accumulation of collisions, so that thermalization of electron-hole pairs cannot happen on the subpicosecond time scale set by the duration of the THz pulse itself. It is

therefore likely that for the full impact ionization process to take place, a longer time scale is needed, probably in the tens-of-picoseconds range, as previously observed for InSb [34]. Nonetheless, the onset of the impact-ionization phenomenon may provide a qualitative explanation for the small differences between the experimental SW(T) and the predictions of the thermodynamic model for one single Dirac band, i.e., without electron-hole pair formation (full green curve in Fig. 2(c). Future time-resolved THz-pump/THz-probe experiments may provide a deeper insight into the nonlinear phenomena taking part.

IV. CONCLUDING REMARKS

We show that a very simple thermodynamic model within the massive Dirac band dispersion—while disregarding the microscopic details of electronic transport at high fields—can be successfully applied to quantitatively describe the THz saturable-absorption properties of bulk BP. This result is particularly interesting since the relativistic treatment is normally not needed to account for the properties of BP at room temperature and pressure. Due to the unique combination of massive Dirac dispersion and low T_F, THz light can nevertheless be used to drive BP in a high-temperature thermodynamic regime, which has hitherto been confined to cosmology rather than condensed-matter physics. Our findings may have useful consequences for the design of BP-based optoelectronic devices, as well as on the engineering of novel THz nonlinear materials.

ACKNOWLEDGMENTS

This work was supported by the Ministero dell'Istruzione e del Merito (MIUR) through the Progetti di Rilevante Interesse Nazionale (PRIN) project No. 2017BZPKSZ. S.L. was supported by MIUR through the PRIN project No. 2020RPEPNH and by the Piano Nazionale di Ripresa e Resilienza (PNRR) project No. PE0000023-NQSTI. E.C. acknowledges financial support from the PNRR MUR project Grant No. PE0000023-NQSTI. A.P. acknowledges G. Perucchi for the artwork in Fig. 1.

APPENDIX A: SAMPLE

High-quality BP crystalline samples with a purity >99.995% were purchased from HQ Graphene (www.hqgraphene.com). The sample was cleaved with Scotch tape until reaching a final thickness of $d = 30 \pm 10$ μm, as measured with a caliper. The sample was then quickly glued onto a sample holder and mounted in the TeraFERMI setup, where it was kept under N_2 purging conditions ($\leqslant$ 3% humidity) during the whole measurement.

APPENDIX B: THE TERAFERMI THz SOURCE

The THz source used for the THz electric field dependent measurements is the TeraFERMI superradiant THz beam line at the FERMI free-electron-laser facility [16,17]. TeraFERMI employs subpicosecond electron bunches in the nanocoulomb range to emit THz light through the coherent-transition-radiation mechanism induced by a 1-μm-thick Al membrane. THz pulses are generated with a repetition rate of 50 Hz and are then guided from the source in vacuum to the TeraFERMI end station, exploiting the high-peak electric fields for nonlinear spectroscopy.

The spectrum of the source is acquired through EOS. We report in Fig. 3 the time profile as well as the spectral content of the pulse, as the squared amplitude of the Fourier transform. The intensity of the THz pulses was measured by utilizing a pyroelectric detector previously calibrated with a GENTEC THZ12D power meter. The maximum intensity measured at sample position was $I = 9$ μJ. The spatial profile was characterized with the help of a Pyrocam III THz camera, yielding a radius $r = 305$ μm. The pulse length is approximated from the measured THz electric field time trace with a Gaussian fit of its intensity (squared electric field). The maximum electric field strength is then estimated also assuming a Gaussian spatial intensity distribution with an area of $A = \pi r^2$:

$$E_0 = \sqrt{\frac{\eta I 2 ln(2)}{\pi r^2 \Delta t}} = 1.65 \text{ MV/cm}, \tag{B1}$$

where $\eta = 377\ \Omega$ is the free-space impedance.

APPENDIX C: EXPERIMENTAL

The THz-field-dependent optical conductivity data are extracted from a transmission experiment performed at different fluences of the incoming THz beam. To this aim, we attenuate the THz pulses with a set of three photolithographic polarizers (from QMC Instruments and Tydex). The first and third polarizers are kept at the same orientation, while the central one is allowed to rotate (at an angle θ_i), thereby attenuating the electric field according to the Malus law.

The THz light transmitted by the BP sample is detected with an electro-optic sampling (EOS) setup, based on a 1-mm-thick ZnTe crystal and a 79.9 MHz C-Fiber780 laser from MENLO, optically synchronized to the FERMI master clock. As a reference, we measure the EOS signal (with the same ZnTe crystal) with an empty sample holder, after strongly attenuating the signal with the polarizers (approximately 5×10^{-2}) to the angle $\theta_{\min}$, corresponding to the lowest THz intensity in the present experiment.

The reference EOS trace is scaled with the peak value recorded in EOS measurements performed for all attenuation angles with a GaP 100-μm-thick crystal instead of

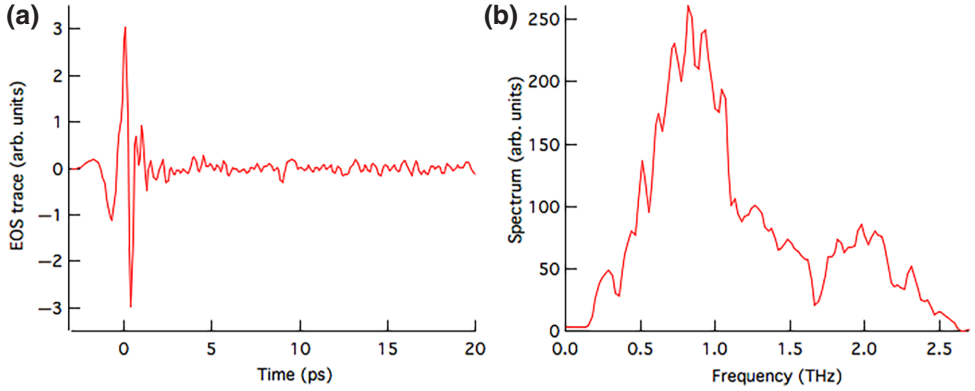

FIG. 3. (a) A representative THz time trace of the source and (b) the corresponding intensity spectrum.

ZnTe:

$$E^{\mathrm{ref},\theta_i}(t) = E^{\mathrm{ref},\theta_{\min}}_{\mathrm{ZnTe}}(t) \cdot \frac{E^{\mathrm{ref},\theta_i}_{\mathrm{GaP}}(t_{\max})}{E^{\mathrm{ref},\theta_{\min}}_{\mathrm{GaP}}(t_{\max})}. \tag{C1}$$

The use of GaP, as a normalization method for the reference spectra, avoids incurring in saturation effects in the more sensitive ZnTe crystal when the THz pulses are not attenuated enough by the polarizers or by the sample itself. This allows us to evaluate the transmission as

$$T_i(t) = E^{\mathrm{BP},\theta_i}_{\mathrm{ZnTe}}(t)/E^{\mathrm{ref},\theta_i}(t). \tag{C2}$$

The real and imaginary parts of the refractive index $\tilde{n}(\nu) = n(\nu) - ik(\nu)$ are evaluated using standard formulas, as described in Ref. [35].

The real part of the optical conductivity is finally evaluated through

$$\sigma_1(\nu) = \frac{1}{4\pi} 2n(\nu)k(\nu). \tag{C3}$$

The optical conductivities, extracted as discussed above, are fitted between $\nu = 0.5$ and 2.5 THz, by employing a simple Drude model:

$$\sigma_1(\nu) = \frac{1}{4\pi} \frac{\omega_p^2}{\Gamma^2 - (2\pi\nu)^2}. \tag{C4}$$

Figure 5 reports on the optical conductivity measured along both the *armchair* (blue) and *zig-zag* (red) polarization directions. In the case of *zig-zag* polarization, a less-pronounced saturable-absorption behavior is found if compared with the case of *armchair* direction. This result can be qualitatively understood by considering the reduced anharmonicity of the *zig-zag* band dispersion with respect to the Dirac-like *armchair* polarization, as discussed in the main text.

APPENDIX D: TEMPERATURE-DEPENDENT FTIR REFLECTIVITY DATA

Temperature-dependent reflectivity measurements were performed on a bulk sample from the same batch as the one used for the THz-field-dependent measurements. A bulk freshly cleaved sample was mounted on a Helitran LT-s He-flux cryostat equipped with different optical windows (polyethylene and KRS5 for the far-infrared and midinfrared ranges, respectively). The measurements were performed at the SISSI infrared beam line [18], at nearly normal incidence, by employing a Bruker Vertex 70v FTIR spectrometer, equipped with suitable beam splitters (Si, KBr) and detectors (Si bolometer, MCT photodetector). A linear polarizer was inserted in the optical path to select the response from the *armchair* direction. Such an orientation is selected by maximizing the reflectivity in the far-infrared range. As a reference for the reflectivity

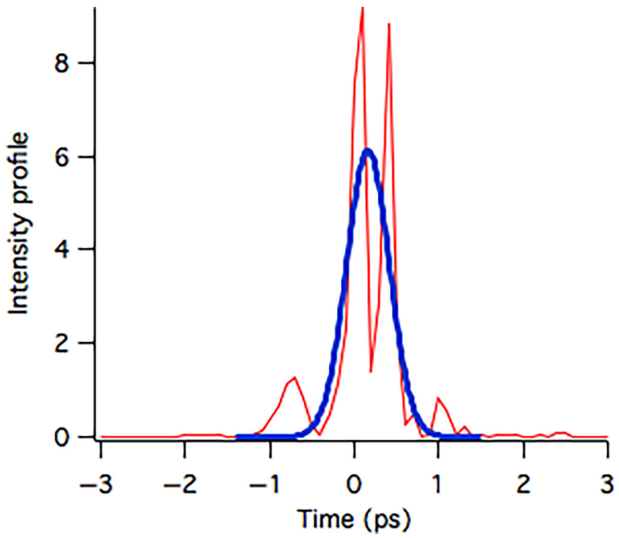

FIG. 4. The Gaussian fit of the intensity time profile. The pulse duration is estimated as $\Delta t = 590$ fs FWHM.

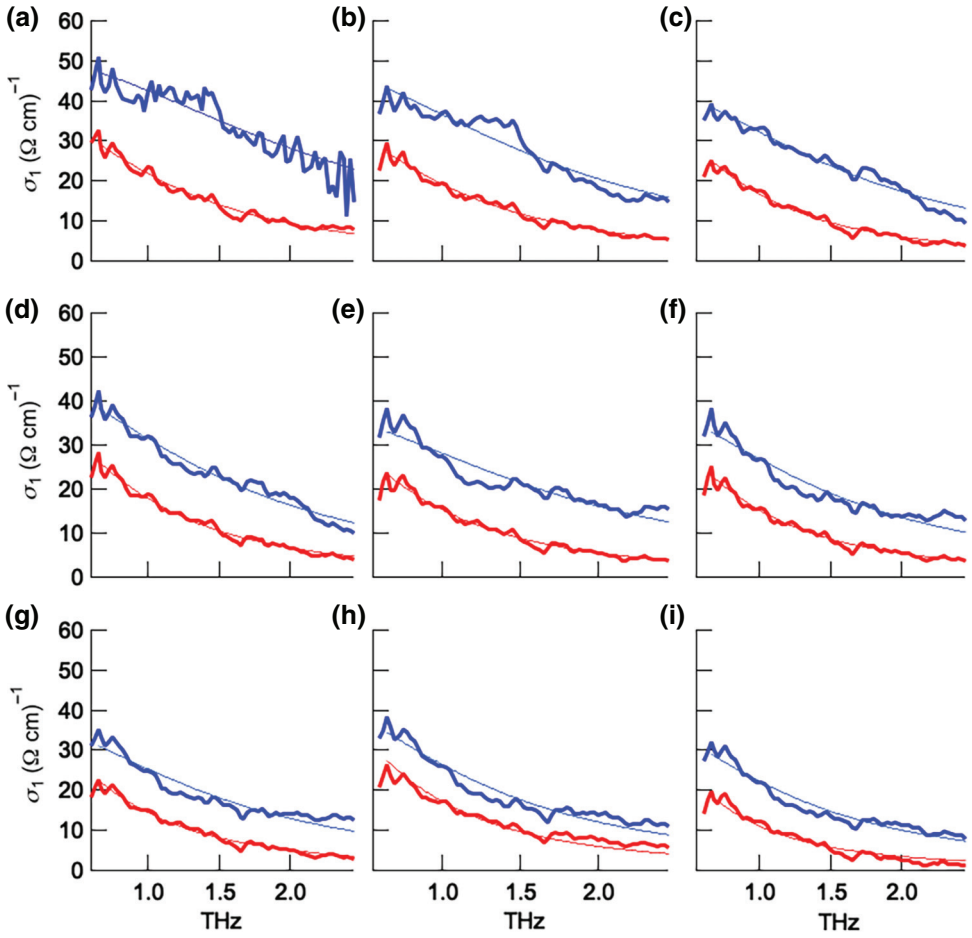

FIG. 5. The real part of the optical conductivity, at all measured electric field values along the *armchair* (blue) and *zig-zag* (red) polarization directions: (a) 350, (b) 450, (c) 690, (d) 920, (e) 1140, (f) 1220, (g) 1390, (h) 1470, and (i) 1650 kV/cm. The lighter lines correspond to the Drude fittings.

measurement, we employ the gold-overcoating technique [36].

The optical reflectivity data are extrapolated at low and high frequencies using standard procedures, in order to extract the optical conductivity through Kramers-Kronig transformations [37]. The THz optical conductivity is fitted with the help of the Drude model, as in Eq. (C4), thus allowing us to establish the temperature dependence of the plasma frequency $\omega_p(T)$ and the scattering rate $\gamma(T)$.

From the value of the plasma frequency $\omega_p(T)$ and by using an effective-mass value of $m^*/m_e = 0.08$ from the literature for the *armchair* direction [38,39], it is possible to calculate the charge density:

$$N = \frac{\omega_p^2 m^*}{4\pi e^2} = 5.8 \times 10^{17}\ \mathrm{cm}^{-3}. \tag{D1}$$

The Fermi energy can be then estimated through

$$\varepsilon_F = \frac{\hbar^2}{2m^*}(3\pi^2 N)^{2/3} = 31.7\ \mathrm{meV}. \tag{D2}$$

The density of states at the Fermi level is finally given by

$$D(\varepsilon_F) = \frac{3}{2}\frac{N}{\varepsilon_F} = 1.71 \times 10^{44}\ \mathrm{J}^{-1}\ \mathrm{m}^{-3}. \tag{D3}$$

APPENDIX E: NONLINEAR FDTD MODEL

A one-dimensional FDTD method based on the Yee algorithm together with the model of the ballistic motion of conduction electrons, as presented in Ref. [21], can be used to describe the intense THz-pulse-induced transparency observed in the bulk BP, in semiquantitative agreement with experiment. According to this model, under the intense THz field, the electrons are accelerated to the highly nonparabolic regions of the conduction-band energy of BP in the first BZ. The model does not take into account the interband tunneling, impact ionization, or any scattering mechanisms other than those in the Drude model. In this theory, the electric displacement (D) in BP due to the propagation of the THz beam is given by

$$D = \epsilon_0 \epsilon_\infty E_{\mathrm{THz}} + P_{\mathrm{NL}}, \tag{E1}$$

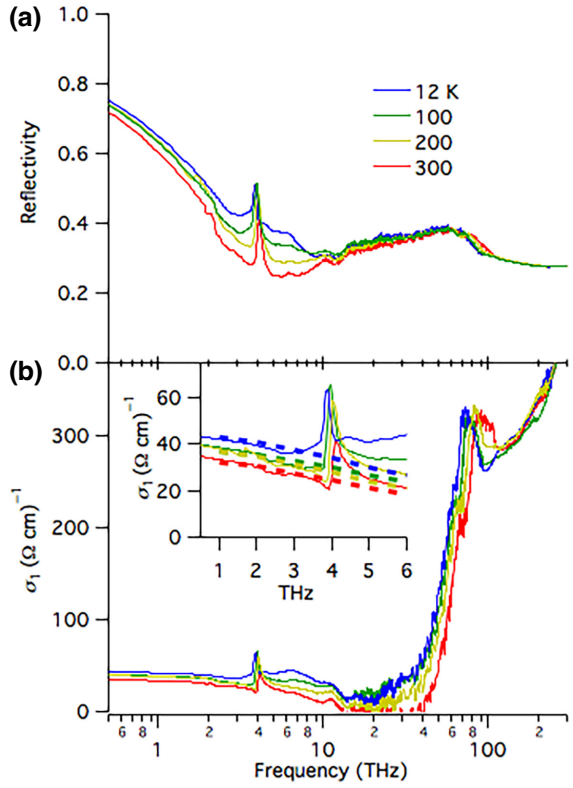

FIG. 6. The temperature-dependent infrared reflectivity (upper panel) and the real part of the optical conductivity (lower panel) as extracted from Kramers-Kronig transformations.

where E_{THz} is the electric field of the THz beam, ϵ_0 is the permittivity of free space, and $\epsilon_\infty = 1 + \chi_0$ is the background dielectric constant, with χ_0 being the background high-frequency dielectric susceptibility. P_{NL} is the nonlinear (NL) polarization arising from the conduction-electron responses to the extreme THz beam. The temporal evolution of the polarization, P_{NL}, is defined as

$$\frac{dP_{\mathrm{NL}}}{dt} = -Nev_g(k), \tag{E2}$$

where $v_g(k)$ is the group velocity of an electron wave packet of wave vector k. Using a semiclassical description, $v_g(k)$ is given by

$$v_g(k) = \frac{1}{\hbar}\frac{\partial \varepsilon(k)}{\partial k}, \tag{E3}$$

where $\varepsilon(k)$ is the conduction-band energy-momentum dependence. The temporal evolution of wave vector k is governed by the equation of motion of the electron in the response to the THz electric field,

$$\frac{dk}{dt} + \Gamma k = \frac{e}{\hbar}E(z,t), \tag{E4}$$

where Γ is the electron scattering rate in the linear regime. In Eq. (E2), n is the carrier density, which is obtained from the plasma-frequency relation with the electron density n and the electron effective mass m^*, i.e., $\omega_p^2 = Ne^2/(\epsilon_0\epsilon_\infty m^*)$. The FDTD method is used to solve the time-dependent Maxwell equations for the propagating THz electromagnetic fields (E, D, and H) inside the BP slab of thickness $d = 30\mu$m. First, H and D are calculated by solving the Maxwell curl equations for a propagating THz field using the Yee central-difference FDTD algorithm at time step $n + 1$, employing the values at the earlier time steps. Then, the electric field E for time step $n + 1$ at each point on the spatial grid s of the position of the BP slab is given by

$$E_s^{n+1} = D_s^{n+1}P_{\mathrm{NL}}^{n+1}/\epsilon_\infty\epsilon_0. \tag{E5}$$

The value of the polarizability at time step $n + 1$, P_{NLs}^{n+1}, is calculated as follows. First, the wave vector k^{n+1} is calculated by solving the differential in Eq. (E4), in the Yee FDTD algorithm. Second, the group velocity, v^{n+1}, corresponding to the value of the wave vector, k^{n+1}, is determined from the realistic conduction-band structure of BP through Eq. (E3). Having the value of v^{n+1}, the polarizability at time step $n + 1$ can be obtained by solving the differential equation of Eq. (E2). For calculating the values at time step $n + 1$, we need to use the stored values from two time steps earlier, $n - 1$, fulfilling the central-difference nature of the Yee FDTD algorithm, where the finite-difference equations are central about the time point t^n. The electric field in free space at time step $n + 1$ can be calculated using $E_s^{n+1} = D_s^{n+1}/\epsilon_0$.

In the simulations, the values for Γ and ω_p are extracted from the experimental data and ϵ_∞ and m^* are given from the literature. The time step Δt is set to 0.5 fs and the spatial step Δz is set to 0.3 μm. All the parameters used in the FDTD simulations are listed in Table I.

TABLE I. The parameters used in the simulation.

ω_p	660 cm^{-1} $\cong$ 19.79 THz
Γ	72.8 cm^{-1} $\cong$ 2.18 THz
m^* ($m_0 = 9.1 \times 10^{-31}$ kg)	0.076 m_0 [40]
ϵ_∞	9.7

According to the model, if the electron moves in a perfectly parabolic potential, the nonlinear polarization component P_{NL} vanishes according to Eqs. (E2) and (E3). On the other hand, when the THz fields are intense enough so as to drive electrons in anharmonic regions of the band dispersion nonlinear effects can no longer be neglected.

This scenario can also be understood in terms of a wave-vector-dependent effective mass. While for a parabolic potential $m^* = \hbar^2(\partial^2\varepsilon/\partial k^2)^{-1}$ is a constant, in the case of anharmonicity, $m^* = m^*(k)$ [see Fig. 7(a)]. In most realistic cases, the electrons then start exploring regions of the BZ, where the band dispersion flattens with respect to the band bottom, thereby resulting in an increased effective

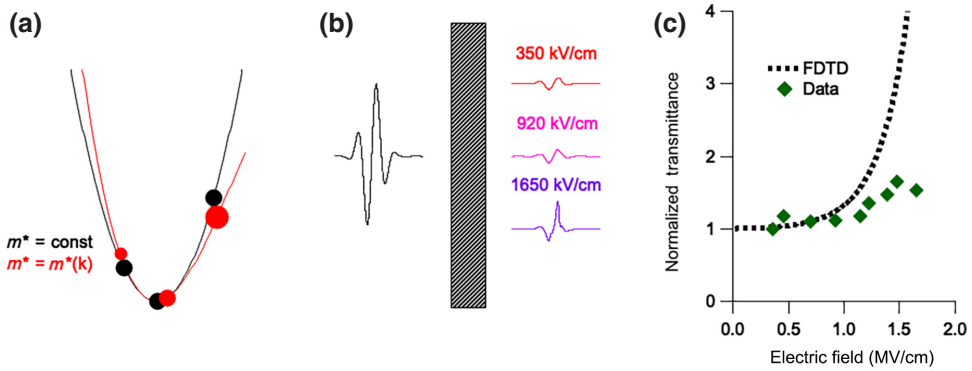

FIG. 7. (a) The schematics of the wave-vector-dependent mass variation. In a nonparabolic potential - such as the one depicted here in red - m^* depends on wavevector k, while m^* is a constant for parabolic bands. (b) The incoming and transmitted THz fields from the BP sample from the FDTD calculation. The outcoming THz fields are normalized to the incoming peak value. With increasing incoming THz fields, the transmitted pulses also increase, thereby qualitatively reproducing the experimentally observed saturable absorption. (c) The THz-field dependence of the transmittance (measured at peak position), defined as $E_{\text{out}}^{\max}/E_{\text{in}}^{\max}$ and normalized to the lowest field value, for both FDTD and experiment.

mass $m^* = m^*(k)$ and saturable-absorption behavior takes place. In the case of BP, the nonlinear FDTD calculation qualitatively reproduces the enhancement of transmitted THz pulses for increasing incoming fields. However, for fields higher than 1 MV/cm, the FDTD simulation strongly overestimates the expected transmitted intensity reduction [see Figs. 7(b) and 7(c)].

APPENDIX F: TWO-TEMPERATURE-MODEL CALCULATION

The calculation of the electron temperature T_e reached after THz photoexcitation has been performed with the NTMpy software package [27], based on a two-temperature model. The model assumes that two independent reservoirs (T_e for electrons and T_l for the lattice) are present and exchange heat after absorption of the THz pulse. This takes place through the coupled differential equations:

$$c_e \rho^{\text{BP}} \frac{\partial T_e}{\partial t} = G(T_l - T_e) + S(t), \tag{F1}$$

$$c_l \rho^{\text{BP}} \frac{\partial T_l}{\partial t} = G(T_e - T_l), \tag{F2}$$

where

(1) $c_e = \gamma_e T_e/\rho^{\text{BP}}$ is the electron heat capacity, with $\gamma_e = \frac{1}{3}\pi^2 D(\varepsilon_F) k_B^2$

(2) $c_l = 9nk_B(T/\theta_{\text{Debye}})^3 \int_0^{\theta_{\text{Debye}}/T} x^4 e^x dx/(e^x - 1)^2$ is the lattice heat capacity

(3) $G = 3\gamma_e \lambda_{e\text{-ph}} E_{\text{Debye}}^2/\pi\hbar k_B$ is the electron-phonon coupling constant

(4) $S(t)$ corresponds to the heat provided by the THz pulse, which is considered here as a Gaussian

with $\rho^{\text{BP}} = 2600$ kg/m^3 and $\theta_{\text{Debye}} = 267$ K ($E_{\text{Debye}} = 0.023$ eV). $n = 5.3 \times 10^{28}$ m^{-3} is the density of ions in the crystal. $\lambda_{e\text{-ph}}$ is the electron-phonon coupling constant.

The code calculates the time-evolution of T_e and T_l as a function of time and for the various BP layers along the full 30-μm-thick stack, by taking into account the absorption of the THz beam at the various layers. A weighted average is finally performed to calculate an effective $T_e(t) = \Sigma_z a_z T_e^z(t)/\Sigma_z a_z$ by multiplying the electronic temperature of each layer by a coefficient $a_z = \exp(-z/z_0)$, where z_0 is the penetration depth at 1 THz.

As thoroughly discussed in Ref. [41], the most reliable experimental technique to evaluate the electron-phonon coupling constant $\lambda_{e\text{-ph}}$ is through *pump-probe* experiments. In order to provide an estimate for $\lambda_{e\text{-ph}}$, we first run the NTMpy code on the time-resolved measurement from Ref. [3]. To this aim, we employ the same material parameters as discussed above while trying different values for $\lambda_{e\text{-ph}}$. It turns out that $\lambda_{e\text{-ph}} \sim 0.1$ provides a relaxation time in quite good agreement with respect to the time-resolved reflectivity data. On the other hand, for $\lambda_{e\text{-ph}}^{\min} = 0.01$ or $\lambda_{e\text{-ph}}^{\max} = 0.2$, the results provided by the NTMpy code start showing some deviations in the relaxation behavior with respect to the experiment.

Once the electron-phonon coupling constant $\lambda_{e\text{-ph}}$ has been established, we can finally apply the code to estimate the electronic temperature T_e in the present experiment. To this aim, we simulate our source with a Gaussian with $\Delta t^{\text{FWHM}} = 590$ fs. The fluence varies from 1.4 to 30.8 J/m^2. We take as a central frequency ν_0 of our source $S(\nu)$ the first moment

$$\nu_0 = \frac{\int \nu S(\nu) d\nu}{\int S(\nu) d\nu} = 1.13 \text{ THz}. \tag{F3}$$

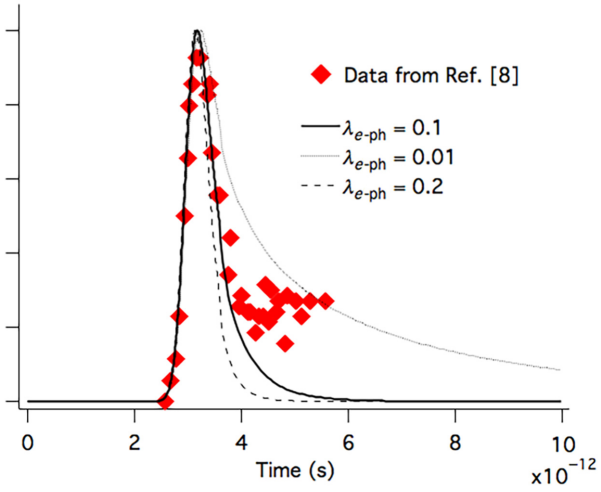

FIG. 8. Time-resolved reflectivity data from Ref. [3] and corresponding simulations performed with the NTMpy code, by using the same material parameters as discussed above, and for different values of the electron-phonon coupling constant $\lambda_{e\text{-ph}}$. It is clear that $\lambda_{e\text{-ph}}\sim 0.1$ properly reproduces the experimental findings and notably the short relaxation within approximately 1 ps.

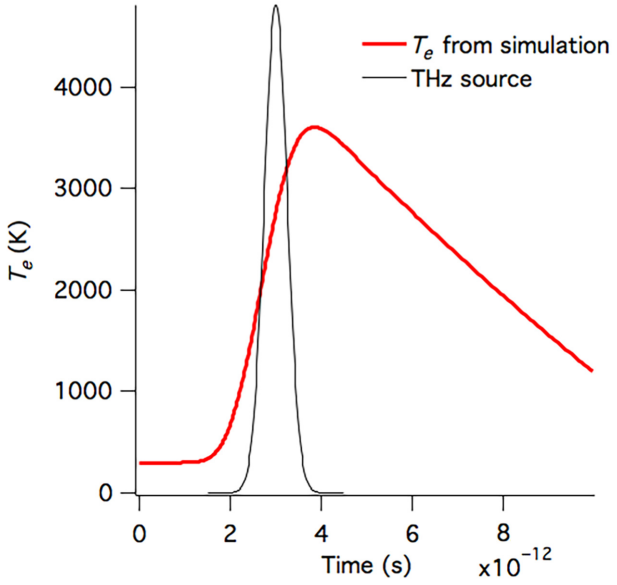

FIG. 9. The time-dependent electronic temperature $T_e(t)$, calculated at the highest fluence for a Gaussian THz source centered at 3 ps (see text).

We finally obtain $\lambda_0 = c/\nu_0 = 295\ \mu$m. With these parameters, we calculate $T_e(t)$, as reported in Fig. 9. In our experiment, we address the nonlinear electrodynamic properties as a function of the THz fluence. This implies that we are only interested in $T_e(t)$ values that are being probed by the THz pulse itself. To this aim, we calculate an effective electronic temperature

$$T_e = \frac{\int T_e(t)S(t)dt}{\int S(t)dt} \tag{F4}$$

at each fluence and for both orientations. These are the temperature values employed in Fig. 2.

APPENDIX G: TEMPERATURE DEPENDENCE OF SPECTRAL WEIGHT

Because of charge conservation, the chemical potential can be defined as the value satisfying the normalization condition [42]:

$$N = \int \frac{1}{4\pi^3} f\left(\varepsilon(\mathbf{k})\right) \mathrm{d}\mathbf{k}, \tag{G1}$$

where

$$f\left(\epsilon(\mathbf{k})\right) = \frac{1}{e^{[\varepsilon(\mathbf{k})-\mu(T)]/k_BT}+1}. \tag{G2}$$

Once N is known, it is possible to numerically evaluate the full temperature dependence of $\mu(T)$ for any possible energy-band dispersion $\varepsilon = \varepsilon(\mathbf{k})$. We report in Fig. 10(b) the temperature dependence of $\mu(T)$ for two different band dispersions: one parabolic band dispersion (red) $\varepsilon(k) = \hbar^2k^2/2m$, with $m = 0.08 \cdot m_e$, and a relativistic Dirac band dispersion (green) in the form $\varepsilon(k) = \sqrt{m^2c^4 + \hbar^2c^2k^2}$, with $m = 0.08 \cdot m_e$ and $c = 4.7 \times 10^5$ m/s, as fits to the BP band structure along the *armchair* direction. For both dispersions, the chemical potential rapidly decreases with temperature and is already crossing the conduction-band bottom at about 350 K and 300 K for parabolic and Dirac dispersions, respectively. While the trend of the chemical potential is quite similar for the two dispersions, the difference in the behavior of the SW, as seen in [Fig. 10(c)], is remarkable. For the parabolic potential, the SW remains constant at all temperatures, while it dramatically decreases and saturates close to 0 for the Dirac dispersion.

Interestingly, if we include the presence of a valence band that is symmetric with respect to the conduction band, the situation drastically changes both from the point of view of the chemical potential and from that of the SW. We have performed the calculation (green dashed line) in the case of the Dirac dispersion by assuming a gap of 0.3 eV (independent of the value of m). In this case, $\mu(T)$ first drops, similarly to what is observed for the single band calculation, and then saturates for an energy of -0.15 eV, corresponding to the center of the gap. From the point of view of the SW, in correspondence with the saturation, we observe an upturn of SW(T), which asymptotically increases linearly with T, as a consequence of the T-induced formation of electron-hole pairs.

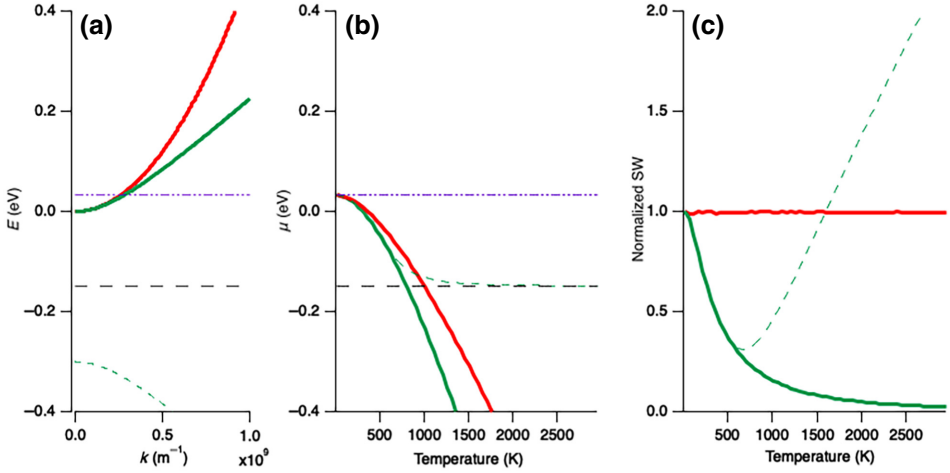

FIG. 10. (a) The energy dispersion for three different energy-band dispersions and the correspondingly calculated (b) chemical potential $\mu(T)$ and (c) spectral weight SW(T). The red lines correspond to parabolic dispersion, while the green lines correspond to massive Dirac dispersion when the conduction band only is taken into account. The dashed green lines correspond to massive Dirac dispersion for symmetric conduction and valence bands with a 0.3-eV gap, thus allowing the formation of electron-hole pairs. The purple dashed-dotted line indicate the Fermi level, while the dashed black line shows the center of the gap.

[1] Z. J. Xiang, G. J. Ye, B. Lei, N. Z. Wang, K. S. Yang, D. Y. Liu, F. B. Meng, X. G. Luo, L. J. Zou, Z. Sun, Y. Zhang, and X. H. Chen, Pressure-induced electronic transition in black phosphorus, Phys. Rev. Lett. **115**, 186403 (2015).

[2] P. Di Pietro, M. Mitrano, S. Caramazza, F. Capitani, S. Lupi, P. Postorino, F. Ripanti, B. Joseph, N. Ehlen, A. Grüneis, A. Sanna, G. Profeta, P. Dore, and A. Perucchi, Emergent Dirac carriers across a pressure-induced Lifshitz transition in black phosphorus, Phys. Rev. B **98**, 165111 (2018).

[3] A. Montanaro, F. Giusti, M. Zanfrognini, P. Di Pietro, F. Glerean, G. Jarc, E. M. Rigoni, S. Y. Mathengattil, D. Varsano, M. Rontani, A. Peucchi, E. Molinari, and D. Fausti, Anomalous non-equilibrium response in black phosphorus to sub-gap mid-infrared excitation, Nat. Commun. **13**, 2667 (2022).

[4] X. Ling, H. Huang, and M. S. Dresselhaus, The renaissance of black phosphorus, Proc. Natl. Acad. Sci. **112**, 4523 (2015).

[5] T. Low, R. Roldàn, H. Wang, F. Xia, P. Avouris, L. M. Moreno, and F. Guinea, Plasmons and screening in monolayer and multilayer black phosphorus, Phys. Rev. Lett. **113**, 106802 (2014).

[6] R. Fei, A. Faghaninia, R. Soklaski, J.-A. Yan, C. Lo, and L. Yang, Enhanced thermoelectric efficiency via orthogonal electrical and thermal conductances in phosphorene, Nano Lett. **14**, 6393 (2014).

[7] S. Biswas, W. S. Whitney, M. Y. Grajower, K. Watanabe, T. Taniguchi, H. A. Bechtel, G. R. Rossman, and H. A. Atwater, Tunable intraband optical conductivity and polarization-dependent epsilon-near-zero behavior in black phosphorus, Sci. Adv. **7**, eabd4623 (2021).

[8] W. Li, B. Chen, C. Meng, W. Fang, Y. Xiao, X. Li, Z. Hu, Y. Xu, L. Tong, H. Wang, W. Liu, J. Bao, and Y. R. Shen, Ultrafast all-optical graphene modulator, Nano Lett. **14**, 955 (2014).

[9] K. J. H. Peters and S. R. K. Rodriguez, Exceptional precision of a nonlinear optical sensor at a square-root singularity, Phys. Rev. Lett. **129**, 013901 (2022).

[10] L. Li, Y. Yu, G. J. Ye, Q. Ge, X. Ou, H. Wu, D. Feng, X. H. Chen, and Y. Zhang, Black phosphorus field-effect transistors, Nat. Nanotechnol. **9**, 372 (2014).

[11] H. Wang, X. Wang, F. Xia, L. Wang, H. Jiang, Q. Xia, M. L. Chin, M. Dubey, and S. Han, Black phosphorus radio-frequency transistors, Nano. Lett. **14**, 6424 (2014).

[12] S. Das, M. Demarteau, and A. Roelofs, Ambipolar phosphorene field effect transistor, ACS Nano **8**, 11730 (2014).

[13] F. Ahmed, Y. D. Kim, Z. Yang, P. He, E. Hwang, H. Yang, J. Hone, and W. J. Yoo, Impact ionization by hot carriers in a black phosphorus field effect transistor, Nat. Commun. **9**, 3414 (2018).

[14] F. Giorgianni, *et al.*, Strong nonlinear terahertz response induced by Dirac surface states in Bi_2Se_3 topological insulator, Nat. Commun. **7**, 11421 (2016).

[15] H. A. Hafez, S. Kovalev, K.-J. Tielrooij, M. Bonn, M. Gensch, and D. Turcinovich, Terahertz nonlinear optics of graphene: From saturable absorption to high-harmonics generation, Adv. Opt. Mater. **8**, 1900771 (2020).

[16] A. Perucchi, S. Di Mitri, G. Penco, E. Allaria, and S. Lupi, The TeraFERMI terahertz source at the seeded FERMI free-electron-laser facility, Rev. Sci. Instr. **84**, 2 (2013).

[17] P. Di Pietro, N. Adhlakha, F. Piccirilli, L. Capasso, C. Svetina, S. Di Mitri, M. Veronese, F. Giorgianni, S. Lupi, and A. Perucchi, TeraFERMI: A superradiant beamline for THz nonlinear studies at the FERMI free electron laser facility, Sync. Rad. News **30**, 36 (2017).

[18] S. Lupi, A. Nucara, A. Perucchi, P. Calvani, M. Ortolani, L. Quaroni, and M. Kiskinova, Performance of SISSI, the infrared beamline of the ELETTRA storage ring, J. Opt. Soc. Am. B **24**, 959 (2007).

[19] Z. Mics, K.-J. Tielrooij, K. Parvez, S. A. Jensen, I. Ivanov, X. Feng, K. Müllen, M. Bonn, and D. Turcinovich, Thermodynamic picture of ultrafast charge transport in graphene, Nat. Commun. **6**, 7655 (2015).

[20] Y. Liu and P. P. Ruden, Temperature-dependent anisotropic charge-carrier mobility limited by ionized impurity scattering in thin-layer black phosphorus, Phys. Rev. B **95**, 165446 (2017).

[21] S. Yu, K. H. Heffernan, and D. Talbayev, Beyond the effective mass approximation: A predictive theory of the nonlinear optical response of conduction electrons, Phys. Rev. B **95**, 125201 (2017).

[22] S. Houver, L. Huber, M. Savoini, E. Abreu, and S. L. Johnson, 2D THz spectroscopic investigation of ballistic conduction-band electron dynamics in InSb, Opt. Express **27**, 10854 (2019).

[23] Y. Minami, K. Araki, T. D. Dao, T. Nagao, M. Kitajima, J. Takeda, and I. Katayama, Terahertz-induced acceleration of massive Dirac electrons in semimetal bismuth, Sci. Rep. **5**, 5870 (2015).

[24] H. A. Hafez, S. Kovalev, J.-C. Deinert, Z. Mics, B. Green, N. Awari, M. Chen, S. Germanskiy, U. Lehnert, J. Teichert, Z. Wang, K.-J. Tielrooij, Z. Liu, Z. Chen, A. Narita, K. Müllen, M. Bonn, M. Gensch, and D. Turchinovich, Extremely efficient terahertz high-harmonic generation in graphene by hot Dirac fermions, Nature **561**, 507 (2018).

[25] M. M. Jadidi, J. C. König-Otto, S. Winnerl, A. B. Sushkov, H. D. Drew, T. E. Murphy, and M. Mittendorff, Nonlinear terahertz absorption of graphene plasmons, Nano Lett. **16**, 2734 (2019).

[26] P. Di Pietro, N. Adhlakha, F. Piccirilli, A. Di Gaspare, J. Moon, S. Oh, S. Di Mitri, S. Spampinati, A. Perucchi, and S. Lupi, Terahertz tuning of Dirac plasmons in Bi_2Se_3 topological insulator, Phys. Rev. Lett. **124**, 226403 (2020).

[27] L. Alber, V. Scalera, V. Unikandanunni, D. Schick, and S. Bonetti, NTMpy: An open source package for solving coupled parabolic differential equations in the framework of the three-temperature model, ArXiv:2002.04559v1 (2020).

[28] N. Ehlen, B. V. Senkovskiy, A. V. Fedorov, A. Perucchi, P. Di Pietro, A. Sanna, G. Profeta, L. Petaccia, and A. Grüneis, Evolution of electronic structure of few-layer phosphorene from angle-resolved photoemission spectroscopy of black phosphorous, Phys. Rev. B **94**, 245410 (2016).

[29] V. P. Gusynin, S. G. Sharapov, and J. P. Carbotte, Sum rules for the optical and Hall conductivity in graphene, Phys. Rev. B **75**, 165407 (2007).

[30] J. Sabio, J. Nilsson, and A. H. Castro Neto, f -sum rule and unconventional spectral weight transfer in graphene, Phys. Rev. B **78**, 075410 (2008).

[31] R. E. Throckmorton and S. Das Sarma, Failure of Kohn's theorem and the apparent failure of the f -sum rule in intrinsic Dirac-Weyl materials in the presence of a filled Fermi sea, Phys. Rev. B **98**, 155112 (2018).

[32] A. J. Frenzel, C. H. Lui, Y. C. Shin, J. Kong, and N. Gedik, Semiconducting-to-metallic photoconductivity crossover and temperature-dependent Drude weight in graphene, Phys. Rev. Lett. **113**, 056602 (2014).

[33] F. J. Sevilla and O. Piña, Thermodynamics of the relativistic Fermi gas in D dimensions, Phys. A: Stat. Mech. Appl. **482**, 585 (2017).

[34] M. C. Hoffmann, J. Hebling, H. Y. Hwang, K.-L. Yeh, and K. A. Nelson, Impact ionization in InSb probed by terahertz pump–terahertz probe spectroscopy, Phys. Rev. B **79**, 161201(R) (2009).

[35] P. U. Jepsen, Phase retrieval in terahertz time-domain measurements: A "how to" tutorial, J. Infrared Millim. Terahertz Waves **40**, 395 (2019).

[36] C. C. Homes, M. Reedyk, D. A. Cradles, and T. Timusk, Technique for measuring the reflectance of irregular, submillimiter-sized samples, Appl. Opt. **32**, 2976 (1993).

[37] M. Dressel and G. Grüner, *Electrodynamics of Solids: Optical Properties of Electrons in Matter* (Cambridge University Press, Cambridge, 2002).

[38] Y. Liu, T. Low, and P. P. Ruden, Mobility anisotropy in monolayer black phosphorus due to scattering by charged impurities, Phys. Rev. B **93**, 165402 (2016).

[39] S.-I. Narita, S.-I. Terada, S. Mori, K. Muro, Y. Akahama, and S. Endo, Far-infrared cyclotron resonance absorptions in black phosphorus single crystals, J. Phys. Soc. Jpn. **52**, 3544 (1983).

[40] G. Gaddemane, W. G. Vanderberghe, M. L. Van de Put, S. Chen, S. Tiwari, E. Chen, and M. V. Fischetti, Theoretical studies of electronic transport in monolayer and bilayer phosphorene: A critical overview, Phys. Rev. B **98**, 115416 (2018).

[41] P. B. Allen, in *Handbook of Superconductivity*, edited by C. P. Poole, Jr. (Academic Press, New York, 1999).

[42] N. W. Ashcroft and N. D. Mermin, *Solid State Physics* (Saunders College Publishing, Philadelphia, 1976).